Photometric Stereo with Non-Lambertian Preprocessing and Hayakawa Lighting Estimation for Highly Detailed Shape Reconstruction

Georg Radow, Giuseppe Rodriguez, Ashkan Mansouri Yarahmadi, and Michael Breuß

Abstract In many realistic scenarios, the use of highly detailed photometric 3D reconstruction techniques is hindered by several challenges in given imagery. Especially the light sources are often unknown and need to be estimated, and the light reflectance is often non-Lambertian. In addition, when approaching the problem to apply photometric techniques at real-world imagery, several parameters appear that need to be fixed in order to obtain high quality reconstructions. In this work, we attempt to tackle these issues by combining photometric stereo with non-Lambertian preprocessing and Hayakawa lighting estimation. At hand of a dedicated study we discuss the applicability of these techniques for their use in automated 3D geometry recovery for 3D printing.

1 Introduction

Photometric stereo (PS) is a fundamental inverse problem aiming at reconstructing the shape of a three dimensional object based on a set of images acquired under a varying source of light. Under this assumption, the images embed the shape

G. Radow · A. Mansouri Yarahmadi · M. Breuß
BTU Cottbus-Senftenberg
Applied Mathematics Group
Institute for Mathematics
Platz der Deutschen Einheit 1
03046 Cottbus, Germany
e-mail: Radow, Yarahmadi, Breuss@b-tu.de
G. Rodriguez
University of Cagliari
Department of Mathematics and Computer Science
via Ospedale 72
09124 Cagliari, Italy
e-mail: rodriguez@unica.it

and color information of the observed object. Despite its long history in computer vision [49, 50], PS is still a fundamentally challenging research problem due to the unknown reflectance and global lighting effects of real-world objects [41]. For the sake of simplicity, the lighting positions and directions are often assumed to be known across the PS research community [4, 28, 38, 48]. However, the real world applications of PS mostly deal with data represented by images acquired under unknown light conditions; see [5], [11], and [21]. In [21], it was shown that at least 6 differently illuminated images are needed to resolve the light positioning, leading to a successful PS scenario that will be further discussed in the current work.

In an almost parallel paradigm, shape from shading (SfS) aims at solving the modeling inverse problem with a set of assumptions similar to PS, except for the fact that in SfS only a single two dimensional image of the object is at hand [16, 52]. The common assumptions among classic (orthographic) PS and SfS are: *(i)* the illumination in the photographed scene, *(ii)* the light reflectance surface properties, *(iii)* the orthographic projection that is performed by the camera need to be known.

Let us first comment on the camera model employed in our setting. In this context, we note that both SfS and PS allow to employ different camera models. An important example is the use of a perspective camera projection which yields more complex equations than in the orthographic setting; see [8] for a comprehensive introduction to perspective SfS and [28, 33, 44] for examples of works on perspective PS. In this work we adopt a canonical orthographic camera as it is suitable in applications with an object located at a relatively far distance from the camera, compared to the object dimensions. This holds true, in particular, in the dataset we focus on, representing a highly detailed seashell illuminated by sunlight. We have validated by undocumented tests that indeed our application scenario is represented well by the orthographic setting. As another classical choice in the setting employed in this work, we consider a classical illumination model [24, 25] that idealizes the environmental light as parallel beams emanating from a light source located at infinity, *e.g.*, the sun.

As indicated, we will follow the Hayakawa lighting estimation method [21] to compute the lighting directions and to make use of them in PS. As a related but different topic of research, the uncalibrated PS approach [5] aims to resolve lighting and 3D depth information simultaneously, which naturally leads to highly sophisticated problem formulations; see, *e.g.*, [19] where non-convex optimization problems need to be resolved. In the context of this line of research we also mention deep learning approaches like the Lighting Calibration Network and its extensions [12, 14]. However, as it often happens with deep learning approaches, the mechanisms behind the estimation are still largely unclear, even if attempts for an analysis give some useful insights [14]. In this article, we prefer to exploit lighting information directly and to keep in this way the explainability of results. Furthermore, there is certainly a point for estimating lighting directly, if it is feasible, and to keep the whole set-up more simple and tractable compared to uncalibrated PS.

We now make some remarks on the light reflected by the photographed objects. In classic works such as [25], Lambertian light reflectance is the most common model in photometric methods. Lambert's model [31] itself is an idealized model and corresponds to a very matte surface without specular highlights, limiting its ap-

plication in real world scenarios. Hence, extending PS to work with non-Lambertian surfaces has been of interest for its practical use. Concerning the seashell dataset that we consider as a best practice example, we remark that the surface of the seashell shows a degree of roughness that can be well understood by a non-Lambertian representation [34, 35, 45], namely the Oren–Nayar, Blinn–Phong, or Torrance–Sparrow model. Among them, the Oren–Nayar model [34] appears to be a pragmatic choice, as it is a reasonable model for matte non-Lambertian surfaces which has been utilized in computer vision, cf. [27, 46, 47].

With recent advances in deep learning schemes, in contrast to more sophisticated mathematical models [34, 35, 45], a range of data-driven approaches have been introduced to model object reflectance properties [13, 26, 40]. Here, we briefly discuss the applicability of some state-of-the-art reflectance modelling approaches to our setup. The deep PS network [40] may not be applicable to our case, because of its predefined light directions assumption between the training and testing phases, while we consider the sun as a source of light, whose changing position is unknown and needs to be estimated. The convolutional neural network based PS introduced in [26] relaxes the lighting constraint in [40], but it is primarily concerned with modelling isotropic materials, namely glass and plastic, whose reflections are invariant under rotation about the surface normal. This clearly does not conform to our rough object of interest.

Along with [26], the approach [43] proposed a physics based unsupervised learning framework to inversely render the general reflectance properties by removing the fixed light constraint. Here, a permutation of the light directions during the training and testing phases is allowed as it impacts the final reconstructed model. In general, all the methods [26, 40, 43] consider a fixed number of input channels to their learning schemes, that is another major constraint in PS.

In a general PS scenario, one may consider the varying number of input images as different channels of a spectral image, as in case of the three channels corresponding to a RGB image. This reformulation in the structure of the input images requires a flexible deep learning scheme that accepts a varying number of input images, in contrast to those schemes with a fixed number of input channels. The channel constraint is of specific importance in case a convolutional layer is chosen as the input layer of the deep learning scheme.

The model based on a deep fully convolutional network [13] resolves the constraint on the number of input channels by locating a recurrent neural network [51] as the input layer, though the lighting knowledge about the training data is still assumed to be known a priori.

One of the challenges that we face in our current study is to derive the positions and directions of the light source, represented by the sun in an outdoor environment, based only on a set of images of the object. In [22], PS was investigated during a single day under a variety of sunlight conditions obtained from a sky probes dataset [23], but to the best of our knowledge no deep learning scheme addresses an outdoor PS scenario with unknown light sources.

In the following we will discuss Hayakawa's method for estimating light positions [21], as well as a simplified Oren–Nayar approach [34, 39]. Their combination is the main line of the current study.

2 Mathematical Setup

A classical orthographic SfS model [29] with a varying source of light illuminating an approximately Lambertian [34] object are the main elements of our setup. Let us describe them in detail.

We assume a right handed reference system in $\mathbb{R}^3$ along with a camera placed at infinity, performing an orthographic projection such that the z-axis and the optical axis of the camera coincide. A varying light source represented by the vectors

$$\boldsymbol{\ell}_t = (\ell_{1t}, \ell_{2t}, \ell_{3t})^\top, \quad t = 1, \ldots, q,$$

illuminates the object from an infinite distance and from q different directions. Note that $\|\boldsymbol{\ell}_t\|$ is proportional to the light intensity, leading to the introduction of an undetermined proportionality constant to the problem. Here and in the following, $\|\cdot\|$ represents the *Euclidean* norm.

We assume each vector $\boldsymbol{\ell}_t$ emanates from the object to the light source, and that both the normal vectors to the object surface and the light vectors themselves point to the same half-space, determined by the positive direction of the z-axis. Since we will employ the Oren–Nayar model [34] to approximate the observed object by a Lambertian one, the incident angle between the light and the normal vectors will be of our specific interest, as it will be further explained in Section 5.

In this setting, we capture q images, each with horizontal and vertical sides of size A and B, respectively. Each image is considered as the sampling of a function $u(x,y)$, defined on the domain $\Omega = [-A/2, A/2] \times [-B/2, B/2]$, at the points

$$(x_i, y_j) := (-A/2 + ih, -B/2 + jh),$$

letting $i \in \{0, \ldots, r+1\}$, $j \in \{0, \ldots, s+1\}$, $s, r \in \mathbb{N}$, $h = A/(r+1)$ and $B = (s+1)\,h$. The size of the corresponding discretized images is $(r+2) \times (s+2)$.

To each point $(x, y) \in \Omega$, a depth value $u(x, y) \in \mathbb{R}^+$ is associated, with a gradient vector

$$\nabla u\,(x, y) = \left(\frac{\partial u\,(x, y)}{\partial x}, \frac{\partial u\,(x, y)}{\partial y} \right)^\top = (u_x, u_y)^\top, \tag{1}$$

and a normal vector

$$\mathbf{n}(x, y) = \frac{(-u_x, -u_y, 1)^\top}{\sqrt{1 + \|\nabla u\|^2}}. \tag{2}$$

One of the main object of interest in this study is the approximation to a Lambertian surface based on the Oren–Nayar model [34]. This allows one to assume that Lambert's cosine law

$$\rho(x,y)\,\langle \mathbf{n}(x,y), \boldsymbol{\ell}_t \rangle = \mathcal{I}_t(x,y), \quad t = 1, \ldots, q, \tag{3}$$

holds true, where $\langle \cdot, \cdot \rangle$ is the usual inner product in $\mathbb{R}^3$, the light intensity at each point of the tth image is denoted by $\mathcal{I}_t(x,y)$, and the scalar function $\rho(x,y)$ represents the *albedo* at each surface point and keeps into account the partial light absorption of that portion of the surface,

For what follows, it is convenient that the captured images are stored in vector form, so we order their pixels lexicographically. Here, the coordinate pixel $(x_i, y_j) \in \Omega$ is mapped to the index $k = (i-1)\,s + j$, where $k \in \{1, \ldots, p\}$ and $p = (r+2)\,(s+2)$ is the number of image pixels. In the following we will assume $p \gg q$, since the number of pixels in an image is usually very large, while we aim at obtaining a reconstruction using a small set of images. The corresponding vector images are denoted by $\mathbf{m}_1, \mathbf{m}_2, \ldots, \mathbf{m}_q \in \mathbb{R}^p$, and we rewrite the discretization in any of the following forms

$$
\begin{aligned}
u(x_i, y_j) &= u_{i,j} = u_k, \\
u_x(x_i, y_j) &= (u_x)_{i,j} = (u_x)_k, \\
u_y(x_i, y_j) &= (u_y)_{i,j} = (u_y)_k, \\
\mathbf{n}(x_i, y_j) &= \mathbf{n}_{i,j} = \mathbf{n}_k, \\
\mathcal{I}_t(x_i, y_j) &= (\mathbf{m}_t)_k = m_{k,t},
\end{aligned}
$$

depending on the context.

Here is a brief review of our classical assumptions:

- the surface is approximated by a Lambertian one, based on [34, 39];
- the sources of light are placed at infinite distance from the object;
- no shadow is cast on the surface;
- the camera is sufficiently far from the object. resulting in the absence of any perspective deformation.

Under these assumptions, rewriting Lambert's law (3), we obtain

$$\rho(x,y) \left\langle \frac{(-u_x, -u_y, 1)^\top}{\sqrt{1 + \|\nabla u(x,y)\|^2}}, (\ell_{1t}, \ell_{2t}, \ell_{3t})^\top \right\rangle = \mathcal{I}_t(x,y),$$

from which, multiplying both sides by $\sqrt{1 + \|\nabla u(x,y)\|^2} \geq 1$,

$$\mathcal{I}(x,y)\sqrt{1 + \|\nabla u(x,y)\|^2} - \rho(x,y)\left\langle (-u_x, -u_y, 1)^\top, (\ell_{1t}, \ell_{2t}, \ell_{3t})^\top \right\rangle = 0.$$

Next,

$$0 = \mathcal{I}\left(x, y\right) \sqrt{1 + \left\|\nabla u\left(x, y\right)\right\|^2} + \rho\left(x, y\right) \left(\left\langle \nabla u\left(x, y\right), \left(\ell_{1t}, \ell_{2t}\right)^\top \right\rangle - \ell_{3t}\right)$$
$$:= H_t\left(x, y, \nabla u\left(x, y\right)\right) \quad (4)$$

is deduced after performing the scalar product and considering (1).

At any surface point $(x, y, u(x, y)) \in \mathbb{R}^3$, a normal vector $(-\nabla u(x, y), 1)^\top$ is approximated using (4), provided Dirichlet boundary conditions

$$u\left(x, y\right) = g\left(x, y\right), \quad \forall\left(x, y\right) \in \partial\Omega,$$

are addressed, where $\partial\Omega$ denotes the boundary of the domain Ω. In conclusion, one obtains the following Hamilton–Jacobi differential model:

$$\begin{cases} H_t(x, y, \nabla u(x, y)) = 0, & t = 1, \dots, q, \\ u(x, y) = g(x, y), & (x, y) \in \partial\Omega. \end{cases} \quad (5)$$

3 Photometric Stereo with Known Lighting

We recall that, by enforcing the Dirichlet boundary condition on (5), we aim at solving a nonlinear system of q first order partial differential equations of Hamilton–Jacobi type. Assuming that the light directions $\ell_t, t = 1, \dots, q$, are known and following [32], we let $t = 1$ in (3) to obtain

$$\sqrt{1 + \|\nabla u(x, y)\|^2} = \rho(x, y) \frac{\langle -\nabla u(x, y), \tilde{\ell}_1 \rangle + \ell_{31}}{\mathcal{I}_1(x, y)}, \quad (6)$$

with $\tilde{\ell}_t := (\ell_{1t}, \ell_{2t})^\top \in \mathbb{R}^2$. Next, we substitute (6) in the equations corresponding to $t = 2, \dots, q$, obtaining

$$\left(\langle -\nabla u(x, y), \tilde{\ell}_1 \rangle - \ell_{31}\right) \mathcal{I}_t(x, y) = \left(\langle -\nabla u(x, y), \tilde{\ell}_t \rangle - \ell_{3t}\right) \mathcal{I}_1(x, y). \quad (7)$$

The well-posedness of (7) is assured in the case $q \geq 2$, that is, if at least two images are available; see also [36]. In practice, the bigger is q, the more likely we are able to construct a meaningful solution. Indeed, when $q = 2$ the solution may not be inferred if the assumptions on the method are not perfectly verified. On the contrary, a data set with three or more images illuminated from accurately known light sources leads to a least-square problem that effectively reduces the noise influence and results in a better approximation of the depth function $u(x, y)$.

Finally, the albedo is found by the equation

$$\rho(x, y) = \frac{\mathcal{I}_t(x, y)}{\langle \mathbf{n}(x, y), \ell_t \rangle}, \quad \text{for any } t = 1, \dots, q.$$

The conditions for the existence and uniqueness of the solution of (5) have been studied in [30]. The reader is further referred to [32] for a study of the problem at hand with a set of more realistic assumptions. In addition, [42] provides a fundamental treatment of (5) in the PS context.

We stress once again the importance of the lights position, since in certain illuminating conditions the coefficient matrix of the linear system resulting from the discretization of (5) might be singular or severely ill-conditioned. However, a suitable positioning of light sources can resolve the issue.

The above approach is a global one. Alternatively, the classical approach [50] for solving PS is to replace the product of albedo and normal vector with a single vector $\tilde{\mathbf{n}} := \rho\mathbf{n}$. In the following we confine our attention to the subset $\widetilde{\Omega} \subset \Omega$, which corresponds to those locations belonging to the actual object that we want to reconstruct, and not to the background. Then, the solution for each $(x, y) \in \widetilde{\Omega}$ is found locally via

$$\hat{\mathbf{n}} = \underset{\tilde{\mathbf{n}} \in \mathbb{R}^3}{\arg\min} \sum_{t=1}^{q} \left(\langle \tilde{\mathbf{n}}, \boldsymbol{\ell}_t \rangle - \mathcal{I}_t(x, y) \right)^2, \quad \rho(x, y) = \|\hat{\mathbf{n}}\|, \quad \mathbf{n}(x, y) = \frac{\hat{\mathbf{n}}}{\|\hat{\mathbf{n}}\|}. \quad (8)$$

Contrary to the previous approach, the minimization in (8) yields a unique solution if $q \geq 3$ and three light sources must be non coplanar, *cf.* [50].

The normal vectors obtained through (8) are the best local explanation of the sampled images with known lighting, according to Lambert's reflectance model and without considering robustness to noise. However, in general they are not integrable, *i.e.*, they do not correspond to an actual surface. Then, the second step consists of obtaining the depth u through numerical normal integration. Following [37], one approach is to compute u as

$$u = \underset{u}{\arg\min} \iint_{\widetilde{\Omega}} \|\nabla u(x, y) - g_\perp(x, y)\|^2 \, \mathrm{d}x \, \mathrm{d}y \quad \Longleftrightarrow \quad \Delta u = \mathrm{div} g_\perp. \quad (9)$$

We first discuss the construction of $g_\perp : \widetilde{\Omega} \to \mathbb{R}^2$ for the orthographic perspective setting. With n_i, $i = 1, 2, 3$, we refer to the components of a field of normal vectors, *i.e.* $\mathbf{n} = [n_1, \ n_2, \ n_3]^\top$. In the case of orthographic projection, the vector $g_\perp$ is constructed as

$$g_\perp = \left[-\frac{n_1}{n_3}, \ -\frac{n_2}{n_3} \right]^\top. \quad (10)$$

Solving the Poisson equation in (9) requires an adequately chosen boundary condition. Here, we utilize the so-called natural boundary condition $\langle \nabla u - g, \eta \rangle = 0$, with η being the normal vector to $\partial\widetilde{\Omega}$ in the image plane Ω. The implementation of this boundary condition is not trivial, since $\widetilde{\Omega}$ is in general not rectangular. For the technical details we refer the interested reader to [10].

We note that (9) does not yield a unique solution, even with the natural boundary condition. This because to any solution u^* we can add any constant $c \in \mathbb{R}$ such that $u^* + c$ is still a solution. This can be prevented by simply adding the term

$$\lambda \iint_{\widetilde{\Omega}} \|u(x,y)\|^2 \, \mathrm{d}x \, \mathrm{d}y \qquad\qquad (11)$$

to the minimized function in (9), with a small weight $\lambda > 0$, *e.g.*, 10^{-9}. Thus, the resulting solution u^* will be around 0, which does not change its shape drastically.

In contrast to (2), in the perspective projection setting the normal vector depends not only on the spatial derivatives of u, but also on the (positive) depth u itself. A method to circumvent this issue is to deploy an auxiliary variable $\nu := \ln u$. Thus, with focal length f and a carefully chosen normalization factor $1/u$, we obtain

$$\mathbf{n} = \frac{\tilde{\mathbf{n}}}{\|\tilde{\mathbf{n}}\|}, \qquad \tilde{\mathbf{n}} = \frac{1}{u} \begin{bmatrix} -fu_x \\ -fu_y \\ u + xu_x + yu_y \end{bmatrix} = \begin{bmatrix} -f\nu_x \\ -f\nu_y \\ 1 + x\nu_x + y\nu_y \end{bmatrix}.$$

Analogously to (9) and (10), the perspective case leads to

$$\nu = \arg\min_{\nu} \iint_{\widetilde{\Omega}} \|\nabla\nu(x,y) - g_\angle(x,y)\|^2 \, \mathrm{d}x \, \mathrm{d}y \quad \Longleftrightarrow \quad \Delta\nu = \mathrm{div} g_\angle,$$

with

$$g_\angle(x,y) = \begin{bmatrix} -n_1/(xn_1 + yn_2 + fn_3) \\ -n_2/(xn_1 + yn_2 + fn_3) \end{bmatrix}.$$

Again, a more detailed account can be found in [37].

Also in this case, natural boundary conditions and a regularizing term similar to (11) are employed. However, an additive constant for ν translates into a multiplier for $u = \exp(\nu)$, which will usually lead to an incorrectly scaled reconstruction. To mitigate this, we employ the following heuristic. We compute two reconstructions $u_\perp$ and $u_\angle = \exp(\nu_\angle)$ while assuming orthographic and perspective projection, respectively. Then we simply compute the final reconstruction as $u^* = c_1 u_\angle$, where c_1 is the variable obtained through

$$(c_1, c_2)^\top = \arg\min_{(c_1,c_2) \in \mathbb{R}^2} \iint_{\widetilde{\Omega}} \|u_\perp(x,y) - c_1 u_\angle(x,y) + c_2\|^2 \, \mathrm{d}x \, \mathrm{d}y.$$

The result is a perspective reconstruction with the multiplier chosen such that its shape is as close as possible to the orthographic reconstruction.

4 Hayakawa's Lighting Estimation Setup

As already pointed out in Section 2 we restructure the gray input image values as the $p \times q$ data matrix

$$\mathcal{M} = \begin{bmatrix} \mathbf{m}_1 \ \mathbf{m}_2 \ \cdots \ \mathbf{m}_q \end{bmatrix} = \begin{bmatrix} m_{11} & m_{12} & \cdots & m_{1q} \\ m_{21} & m_{22} & \cdots & m_{2q} \\ \vdots & \vdots & & \vdots \\ m_{p1} & m_{p2} & \cdots & m_{pq} \end{bmatrix},$$

where the matrix entry m_{kt} corresponds to the gray value of the kth pixel of the tth input image.

Let

$$\mathcal{R} = \begin{bmatrix} \rho_1 & & 0 \\ & \ddots & \\ 0 & & \rho_p \end{bmatrix},$$

be the surface reflectance diagonal matrix,

$$\mathcal{N} = \begin{bmatrix} \mathbf{n}_1 \ \mathbf{n}_2 \ \cdots \ \mathbf{n}_q \end{bmatrix} = \begin{bmatrix} n_{11} & n_{12} & \cdots & n_{1p} \\ n_{21} & n_{22} & \cdots & n_{2p} \\ n_{31} & n_{32} & \cdots & n_{3p} \end{bmatrix},$$

represent the $3 \times p$ surface normal matrix, and

$$\mathcal{L} = \begin{bmatrix} \boldsymbol{\ell}_1 \ \boldsymbol{\ell}_2 \ \cdots \ \boldsymbol{\ell}_q \end{bmatrix} = \begin{bmatrix} \ell_{11} & \ell_{12} & \cdots & \ell_{1q} \\ \ell_{21} & \ell_{22} & \cdots & \ell_{2q} \\ \ell_{31} & \ell_{32} & \cdots & \ell_{3q} \end{bmatrix},$$

the $3 \times q$ light source directions matrix. Then, we can write a discrete statement of Lambert's law (3) as the matrix equation

$$\mathcal{M} = \mathcal{R}\mathcal{N}^{\top}\mathcal{L}. \tag{12}$$

The photometric stereo technique under unknown lighting consists of computing the rank-3 factorization

$$\mathcal{M} = \widetilde{\mathcal{N}}^{\top}\mathcal{L} \tag{13}$$

where $\widetilde{\mathcal{N}} = \mathcal{N}\mathcal{R}$ (*cf.* (12)), without knowing in advance the lights location, *i.e.*, the matrix $\mathcal{L}$. Here, we briefly recall the method proposed by Hayakawa [21]; see also [15].

Let the compact singular value composition (SVD) [18] of the image data matrix be

$$\mathcal{M} = U\Sigma V^{\top}, \tag{14}$$

where the diagonal matrix

$$\Sigma = \text{diag}(\sigma_1, \ldots, \sigma_q) = \begin{bmatrix} \sigma_1 & & 0 \\ & \ddots & \\ 0 & & \sigma_q \end{bmatrix}$$

contains the singular values $\sigma_1 \geq \cdots \geq \sigma_q \geq 0$, and $U \in \mathbb{R}^{p \times q}$ and $V \in \mathbb{R}^{q \times q}$ are matrices with orthonormal columns $\mathbf{u}_i$ and $\mathbf{v}_i$. These are called the left and right singular vectors, respectively. As already remarked, in real PS applications $q \ll p$.

When q is small, the SVD factorization can be computed efficiently by standard numerical libraries, even for a quite large value of p. In the case of a very large data set, with the aim of reducing the computational complexity, a partial SVD may be constructed at a reduced cost [2, 3].

In (12), we assumed the data matrix $\mathcal{M}$ to have rank 3. In this situation

$$\sigma_1 \geq \sigma_2 \geq \sigma_3 > \sigma_4 = \cdots = \sigma_q = 0.$$

Anyway, since images may be acquired in non-ideal conditions and may be affected by noise, factorization (14) usually has numerical rank $r > 3$. Then, a *truncated* SVD must be performed. This is achieved by adopting the partitioning

$$U = \begin{bmatrix} U_1 \ U_2 \end{bmatrix}, \qquad V = \begin{bmatrix} V_1 \ V_2 \end{bmatrix},$$

where U_1 and V_1 contain the first three columns of U and V, respectively, and letting $\Sigma_1 = \mathrm{diag}(\sigma_1, \sigma_2, \sigma_3)$. Then, we consider the approximation

$$\mathcal{M} \simeq \mathcal{M}_1 = W^\top Z,$$

with $W = \Sigma_1 U_1^\top = [\mathbf{w}_1, \ldots, \mathbf{w}_p]$ and $Z = V_1^\top = [\mathbf{z}_1, \ldots, \mathbf{z}_q]$, which produces the best rank-3 approximation to the data matrix $\mathcal{M}$ in both the Euclidean and the Frobenius norm sense [7].

This initial rank-3 factorization is followed by the solution of the $q \times 6$ least squares problem

$$\min_{\mathbf{g} \in \mathbb{R}^6} \|H\mathbf{g} - \mathbf{e}\|, \tag{15}$$

where $\mathbf{e} = (1, \ldots, 1)^\top \in \mathbb{R}^q$ and $H \in \mathbb{R}^{q \times 6}$ is the matrix whose t^{th} row is defined by

$$\begin{bmatrix} z_{1t}^2 \ z_{2t}^2 \ z_{3t}^2 \ 2z_{1t}z_{2t} \ 2z_{1t}z_{3t} \ 2z_{2t}z_{3t} \end{bmatrix},$$

in terms of the elements of the columns $\mathbf{z}_t$ of Z.

The solution of the optimization problem (15) produces a vector $\mathbf{g}$ containing the entries in the upper triangle of a 3×3 symmetric positive definite matrix G, whose Cholesky factor R normalizes the columns of Z, in the sense that $\|R\mathbf{z}_t\| = 1$, $t = 1, \ldots, q$. The factors in the sought factorization (13) are given by

$$\widetilde{\mathcal{N}} = (R^{-1})^\top W, \qquad \mathcal{L} = RZ;$$

see [21] and [15]. Finally, the matrix $\mathcal{N}$ of the normal vectors is obtained by normalizing the columns of $\widetilde{\mathcal{N}}$, and the normalizing constants are the diagonal entries of the albedo matrix $\mathcal{R}$.

Hayakawa's procedure shows that the light positions can be detected only for $q \geq 6$, *i.e.*, if at least 6 images with different lighting are available. Anyway, factorization (12) is unique up to a unitary transformation, and such a transformation has to be

suitably chosen before proceeding with the normal integration, to ensure that the surface can be represented as an explicit function $z = u(x, y)$. A procedure for determining an acceptable surface orientation and to solve at the same time the so-called *bas-relief ambiguity* was proposed in [15, Section V].

5 The Oren–Nayar Model

The Oren–Nayar model [34] is designed to handle rough objects by modeling surfaces as an aggregation of many infinitesimally small Lambertian patches, called facets. A schematic view of a small portion $d\epsilon$ of a rough surface, made from a small set of facets, is displayed in Fig. 1.

The slope values of all such facets follow a Gaussian probability distribution with standard deviation $\sigma \in [0, +\infty)$, also called the *roughness parameter* of the surface. The main idea proposed in [34] is that each facet contributes to the modeled irradiance value $I_{\text{O-N}}$ according to the Oren–Nayar model, as follows

$$I_{\text{O-N}} = \frac{\rho}{\pi} L_i \cos(\theta_i) (\nu_1 + \nu_2 \sin(\alpha) \tan(\beta) \max(0, \cos(\Phi_r - \Phi_i))), \quad (16)$$

where (see also Fig. 2) ρ represents the facet albedo, L_i the intensity of the point-like light source, θ_i the angle between the surface normal and the light source, and θ_r the angle between the surface normal and the camera direction. In addition, two parameters $\alpha = \max(\theta_i, \theta_r)$ and $\beta = \min(\theta_i, \theta_r)$ represent the maximum and the minimum values of θ_i and θ_r, respectively, and the terms ν_1 and ν_2 depend on the roughness parameter σ

$$\nu_1 = 1 - 0.5 \frac{\sigma^2}{\sigma^2 + 0.33} \qquad \text{and} \qquad \nu_2 = 0.45 \frac{\sigma^2}{\sigma^2 + 0.09}.$$
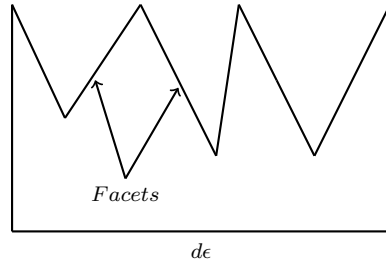

Fig. 1 A schematic side view of a small rough surface $d\epsilon$ formed by a few facets. The surface roughness is characterized by a Gaussian probability distribution of facet slopes with standard deviation $\sigma \in [0, +\infty)$. According to the Oren–Nayar model, each facet contributes to the irradiance value of the surface as shown in (16). Note that, in case of $\sigma = 0$, the surface follows the Lambertian model.
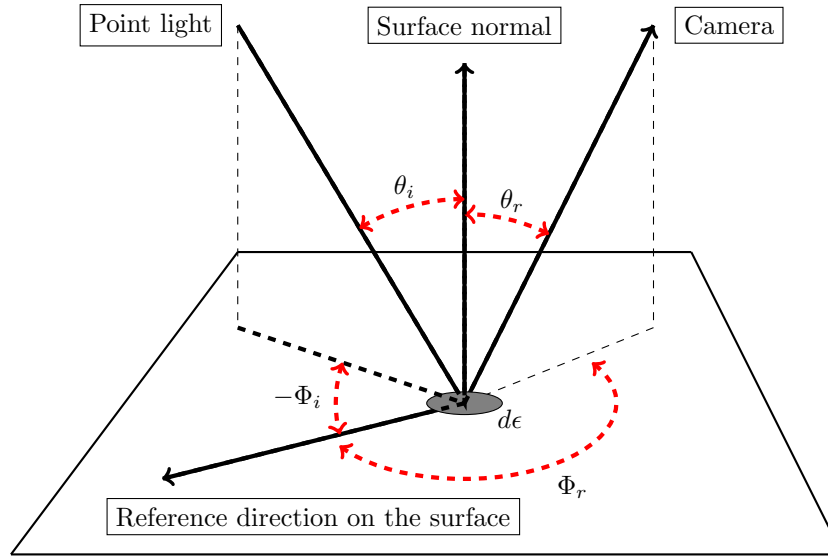
Fig. 2 Illustration of the Oren–Nayar model for the reflectance of a facet being illuminated by a point-like light source and captured by a camera. The directions from which the facet is observed and illuminated determine two angles θ_r and θ_i, respectively, with respect to the normal to the facet. In addition, the reference direction on the surface establishes two azimuth angles Φ_r and Φ_i for the camera and the illumination directions. Note that we do not visualize a particular facet because of its small size $d\epsilon$ compared to the surface area.

Finally, Φ_i and Φ_r denote the azimuth angles for the light source and the camera direction, respectively, with respect to the reference direction on the surface, as shown in Fig. 2.

Next, we assume the point-like light source be located at the optical center of the camera and assume the constant coefficient $\frac{\rho}{\pi} L_i$ in (16) to be normalized to one. The second assumption is not restrictive, as it only depends on the light source intensity, the surface albedo, and the parameters of the imaging system, such as the lens diameter and the focal length; see [1]. This allows us to simplify (16) to

$$I_{\text{O-N}} = \nu_1 \cos(\theta) + \nu_2 \sin^2(\theta), \tag{17}$$

while the light source and viewing directions are considered to be coincident, resulting in $\theta_i = \theta_r = \alpha = \beta = \theta$ and $\Phi_i = \Phi_r$, with $\cos(\Phi_r - \Phi_i) = 1$. In the case of $\sigma = 0$, we have $\nu_1 = 1$ and $\nu_2 = 0$ in (17), and the Oren–Nayar model reduces to the Lambertian one.

A closer look at (17) reveals that the irradiance value $I_{\text{O-N}}$ based on the Oren–Nayar model consists of two components, namely, $\nu_1 \cos(\theta)$, the Lambertian one, and $\nu_2 \sin^2(\theta)$, which is the non-Lambertian component that attains its maximum when $\theta = \frac{\pi}{2}$.

Following the work by [39], we conclude the preprocessing phase by solving (17) for $\cos(\theta)$

$$\cos(\theta) = \frac{\nu_1 \pm \sqrt{\nu_1^2 - 4\nu_2 (I_{\text{O-N}} - \nu_2)}}{2\nu_2}, \tag{18}$$

and considering the solution associated to the minus sign, as motivated in [39]. Note that the obtained Lambertian component $\nu_1 \cos(\theta)$ based on (18) depends on the roughness parameter σ. This fact will be illustrated in our numerical results.

6 Numerical Results

Our data set includes 20 images of a seashell illuminated from different directions by direct sunlight, three of which are shown in Fig. 3. To collect the images, a seashell with a width approximately equal to $10\,(\text{cm})$ was placed face up on a horizontal desk, with a tripod holding a camera about $100(\text{cm})$ above the seashell. The camera has a focal length of $85(\text{mm})$, and a black background was placed below the seashell to reproduce homogeneous Dirichlet boundary conditions for the observed surface. The desk was placed in the open air, under direct sunlight, and rotated in order to obtain 20 different lighting conditions; see Fig. 4. The sun elevation angle was measured at the end of the shooting process; see [15] for a detailed explanation of the shooting procedure and also Fig. 5 for an overview on the modelling pipeline adopted in this work.

In addition, the maximum gray value corresponding to each pixel across all seashell images was determined, to apply a threshold to all of them. This establishes a mask based on a common contribution across all images. Finally, a morphological erosion [20] with a Euclidean disk of radius 3 pixels was used, providing the filtered seashell images for the next step. In this way, we may lose a few shell details on the boundary, but we ensure that there are no parts left in the interface actually belonging to the background. As an additional benefit, sharp peaks in the interface are smoothed.

By considering each seashell to represent a rough surface, we adopt the Oren–Nayar model [34] and approximate the Lambertian component of the seashell surface, namely $\cos\theta$, by formula (18). After performing the computation, all values of $x =$

Fig. 3 Three out of 20 seashell images captured illuminated by sun from different directions, as elaborated in [15].

Fig. 4 Shooting setting for the seashell dataset. The whole system is placed upon a rotating platform.

$\cos\theta$ less than zero and greater than one, namely $-\kappa \leq x < 0$ and $1 < x \leq 1+\kappa$ for a fixed κ, are mapped back to zero and one, respectively, to let the approximated values stay consistently in $[0,1]$. These inaccuracies are introduced by the simplification assumed to derive (17) from (16), making the Oren–Nayar model adoptable in real world applications [34]. In our data set, the Lambertian approximation resulted in values between $[-\kappa, 1]$ with $\kappa = 0.3758$. Out of all approximated Lambertian values, 5.3% were smaller than zero, and none were larger than one.

In Figure 6 we display a selection of the filtered images resulting from our preprocessing pipeline.

In the context of PS under unknown lighting conditions, we applied the procedure proposed in [21] to our masked seashell images to identify the lighting directions by the implementation from [15]. Such a procedure requires at least 6 images to estimate the light positions. As mathematically justified in [15], the resulting algorithm provides the possibility of inferring the lighting directions, leading to a PS problem with known light positions. In [15], a shooting technique was also introduced to solve the so called bas-relief ambiguity [6].

We illustrate in Fig. 7 some results concerning the light positions identified by the software developed in [15] and the corresponding approximated Lambertian models of the seashells, obtained using (18) via orthographic projection for different values of σ. The impact of the roughness parameter σ can be clearly observed in the reconstructed seashells shown in the right column of Fig. 7. Here, each row contains the obtained light directions and a side view of the reconstructed seashell based on the approach proposed in [15]. The roughness parameter σ takes the values $\{1, 8, 25\}$ in degrees, from top to bottom. As it can be observed, larger values of σ cause the light direction to become less steep, and the seashell reconstructions to be more swollen.
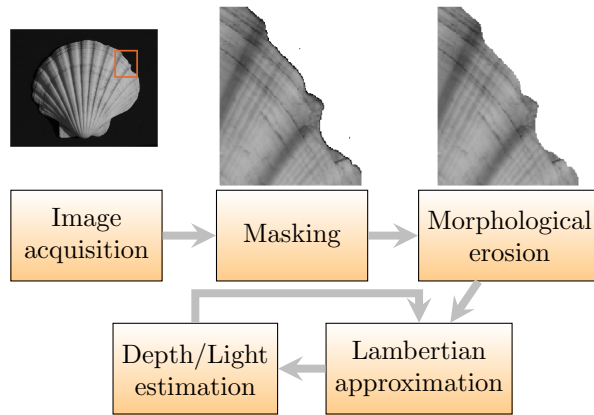
Fig. 5 Workflow adopted in the current work. We start by image acquisition, as explained in [21]. Next, masking and morphological erosion are used as preprocessing phases, so that the Lambertian components of the images can be approximated using the roughness value σ as a free parameter; see [34]. Finally, the optimal σ is found by using an optimization approach [9] that iteratively obtains the light directions and the best seashell model [15]. The optimization performed by [9] is represented by the loop between the last two steps, where σ is varied to produce a new Lambertian approximation, with the aim of producing the values nearest to the ground truth light directions acquired in the image acquisition step.

On the basis of these results, we are motivated to determine a realistic range of variation for σ which results in a set of meaningful 3D reconstructions. In Fig. 8, we plot the residual sum of squares (RSS) between each Lambertian approximation and the corresponding original gray scale image of the seashell, for σ varying in $[\epsilon, 60]$, in degrees. Values larger than $60°$ may not be meaningful in practice; see [34]. The zero value is excluded since in this case the model directly downgrades to a Lambertian one based on (17) and (18) is not applicable any more. The curve shown in Fig. 8 is the mean of the curves corresponding to each of the 20 seashell images, constructed by varying $\sigma \in [\epsilon, 60]$ in steps of one degree. A close observation reveals that a

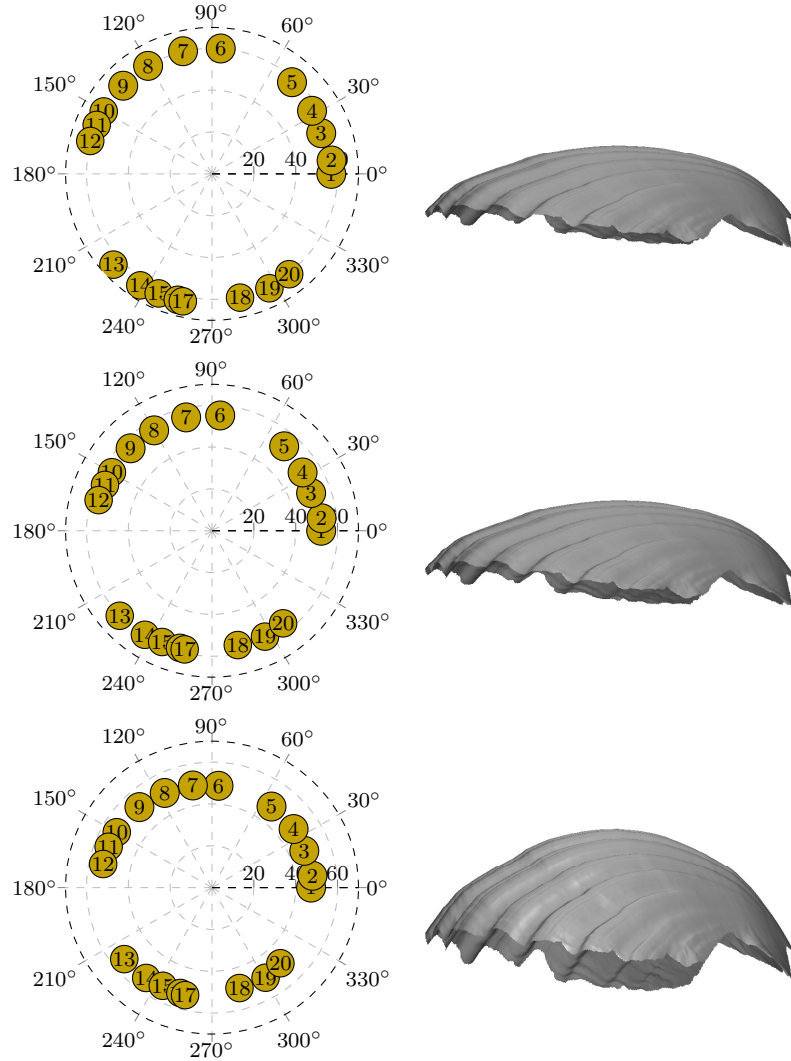**Fig. 6** The filtered versions of the three images shown in Fig. 3.

Fig. 7 The impact of the roughness parameter σ in estimating the light directions and in reconstructing the seashell by the method proposed in [15] can be clearly observed. Here, each row contains the results obtained for the roughness parameter $\sigma = 1°, 8°, 25°$, from top to bottom. A larger value of σ leads to a less steep estimate of the light direction. We observe in the right column a swelling effect on the reconstructed shapes, as a direct consequence of the increase in σ.

value of σ close to $0°$ leads to a relatively high RSS value, revealing the dissimilarity between a grayscale image and its corresponding Lambertian approximation. This is expected, as for $\sigma = 0$ the Oren–Nayar model reduces to the Lambertian one. For $\sigma > 30°$, the curve starts fluctuating and clearly splits into two sub-curves. This motivates us to look for an optimal value of sigma in the range $[1°, 30°]$.
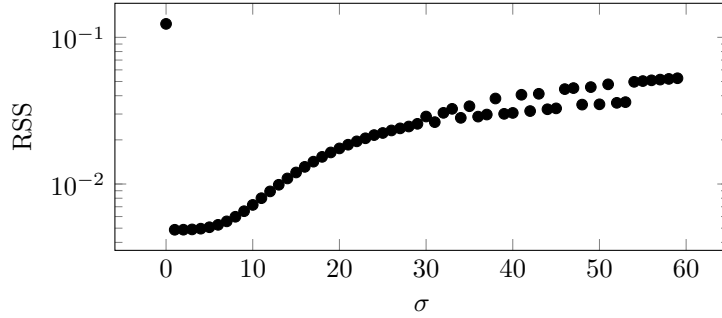
Fig. 8 Variation of the RSS between the Lambertian approximations and the corresponding original gray images of the seashell with values in $[0, 1]$, for σ in $[\epsilon, 60°]$. Here, the RSS is used as a similarity measure. For $\sigma > 30°$ a fluctuation in the RSS is clearly observed, leading to two distinct branches of the curve. When σ is small, a large RSS reveals that the Lambertian modelling of gray images is meaningless. We conclude that a smooth variation of σ in $[1°, 30°]$ justifies the adoption of Oren–Nayar model, motivating us to consider this range as an educated initial guess to look for the optimal σ.
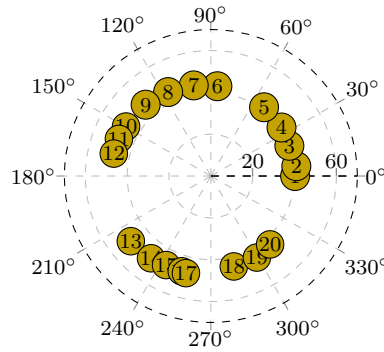
Fig. 9 Azimuth and elevation angles of the light directions estimated according to [15], when the Lambertian approximation corresponds to $\sigma = 21.3795°$. The azimuth angles, in the θ-direction, shed further light on the shooting procedure explained in [15]. Though we expect all the elevation angles, shown in the r-direction, to stay close to the measured ground truth angle $44.4°$, in practice we obtain a range of values in $[40.21°, 49.34°]$.

The $44.4°$ ground truth angle of the sun above the horizon, which can be assumed to be constant for all images since the acquisition time was sufficiently small, is next used to determine σ. In practice, the optimal value proves to be $21.3795°$, after letting σ vary in $[1°, 30°]$ with the aim of obtaining the smallest residual sum of squares (RSS) [17] between the elevation angles of the light directions estimated according to [15] and the ground truth value. This leads us to the inferred model (see Fig. 10) after 16 iterations, with a final RSS value of 171.6720.

The polar graph in Fig. 9 displays the optimal azimuth and elevation angles, estimated by the procedure in [15], for the optimal roughness parameter $\sigma = 21.3795°$. The θ- and r-directions correspond to the azimuth and elevation angles, respectively.

Finally, we report in Fig. 10 the 3D reconstruction based on the light directions represented in Fig. 9, assuming the seashell to be Lambertian with σ equal to $21.3795°$. In particular, we display two views of the reconstructed object, a real picture of the shell, and a depth map of the 3D model.
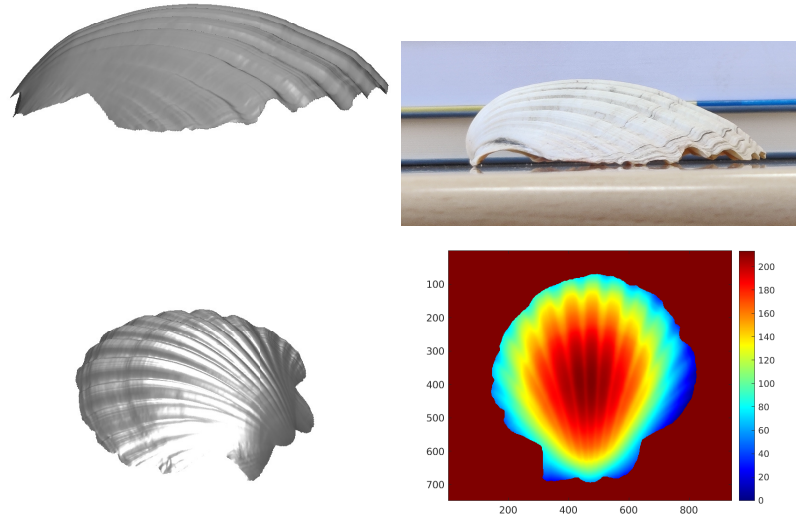

Fig. 10 The top rows displays a side view of the reconstructed surface and a photo of the real shell from the same point of view. In the bottom row we report another view of the reconstructed surface and the depth map of the 3D model of the seashell, by approximating it as a Lambertian surface based on the Oren–Nayar model [34]. The reconstruction is obtained using the light directions shown in Fig. 9.

7 Summary and Conclusion

We developed a novel practical PS pipeline, and we rigorously motivated its constituent components. Our proposed model automatically estimates two fundamental parameters of the model, namely the unknown lighting environment and the reflectance properties of the observed object, whose unavailability often prevent PS to be robustly applied in real-world scenarios. Hayakawa's procedure detects the light positions, provided that at least 6 images of the sample object with different lighting directions are available. In addition, the reflectance properties of a rough object are approximated by the Oren–Nayar model to resemble a Lambertian surface. In practice, the Oren–Nayar model setting is used to tune the Hayakawa's

detected light directions, leading us to achieving the final optimally modelled object, as documented by our numerical results.

Acknowledgements

References

1. Ahmed, A.H., Farag, A.A.: A new formulation for shape from shading for non-Lambertian surfaces. In: Proceedings of the 2006 IEEE Computer Society Conference on Computer Vision and Pattern Recognition (CVPR'06). vol. 2, pp. 17–22. IEEE (2006)
2. Baglama, J., Reichel, L.: Augmented implicitly restarted Lanczos bidiagonalization methods. SIAM Journal on Scientific Computing **27**(1), 19–42 (2005)
3. Baglama, J., Reichel, L.: An implicitly restarted block Lanczos bidiagonalization method using Leja shifts. BIT Numerical Mathematics **53**, 285–310 (2012)
4. Barsky, S., Petrou, M.: The 4-source photometric stereo technique for three-dimensional surfaces in the presence of highlights and shadows. IEEE Transactions on Pattern Analysis and Machine Intelligence **25**(10), 1239–1252 (2003)
5. Basri, R., Jacobs, D., Kemelmacher, I.: Photometric stereo with general, unknown lighting. International Journal of Computer Vision **72**, 239–257 (2007)
6. Belhumeur, P., Kriegman, D., Yuille, A.: The bas-relief abiguity. In: Proceedings of the 1997 IEEE Computer Society Conference on Computer Vision and Pattern Recognition (CVPR'97). pp. 1060–1066. IEEE (1997)
7. Björck, A.: Numerical Methods for Least Squares Problems. Siam Philadelphia (1996)
8. Breuß, M., Yarahmadi, A.M.: Perspective shape from shading. In: Advances in Photometric 3D-Reconstruction. pp. 31–72 (2020)
9. Byrd, R.H., Gilbert, J.C., Nocedal, J.: A trust region method based on interior point techniques for nonlinear programming. Mathematical Programming **89**(1), 149–185 (2000)
10. Bähr, M., Breuß, M., Quéau, Y., Boroujerdi, A.S., Durou, J.D.: Fast and accurate surface normal integration on non-rectangular domains. Computational Visual Media **3**(2), 107–129 (2017)
11. Chen, C.P., Chen, C.S.: The 4-source photometric stereo under general unknown lighting. In: Leonardis, A., Bischof, H., Pinz, A. (eds.) Computer Vision – ECCV 2006. pp. 72–83. Springer Berlin Heidelberg, Berlin, Heidelberg (2006)
12. Chen, G., Han, K., Shi, B., Matsushita, Y., Wong, K.: Self-calibrating deep photometric stereo networks. In: 2019 IEEE/CVF Conference on Computer Vision and Pattern Recognition. pp. 8731–8739 (2019)

13. Chen, G., Han, K., Wong, K.Y.K.: PS-FCN: A flexible learning framework for photometric stereo (2018)
14. Chen, G., Waechter, M., Shi, B., Wong, K.Y.K., Matsushita, Y.: What is learned in deep uncalibrated photometric stereo? In: ECCV (2020)
15. Concas, A., Dessì, R., Fenu, C., Rodriguez, G., Vanzi, M.: Identifying the lights position in photometric stereo under unknown lighting. In: Proceedings of the International Conference on Computational Science and its Applications (ICCSA). Cagliari, Italy (2021), to appear. Preprint available at `arXiv:1809.06933 [math.NA]`
16. Durou, J.D., Falcone, M., Sagona, M.: Numerical methods for shape-from-shading: A new survey with benchmarks. Computer Vision and Image Understanding **109**, 22–43 (2008)
17. Fox, J.: Applied Regression Analysis and Generalized Linear Models. SAGE Publishing (2008)
18. Golub, G.H., Van Loan, C.F.: Matrix Computations. Johns Hopkins University Press, USA (1996)
19. Haefner, B., Ye, Z., Gao, M., Wu, T., Quéau, Y., Cremers, D.: Variational uncalibrated photometric stereo under general lighting. In: Proceedings of the IEEE/CVF International Conference on Computer Vision. pp. 8539–8548 (2019)
20. Haralick, R.M., Sternberg, S.R., Zhuang, X.: Image analysis using mathematical morphology. IEEE Transactions on Pattern Analysis and Machine Intelligence **PAMI-9**(4), 532–550 (1987)
21. Hayakawa, H.: Photometric stereo under a light source with arbitrary motion. Journal of the Optical Society of America A **11**(11), 3079–3089 (1994)
22. Hold-Geoffroy, Y., Gotardo, P., Lalonde, J.F.: Single day outdoor photometric stereo. IEEE Transactions on Pattern Analysis and Machine Intelligence **43**(6), 2062–2074 (Jun 2021). https://doi.org/10.1109/tpami.2019.2962693, http://dx.doi.org/10.1109/TPAMI.2019.2962693
23. Hold-Geoffroy, Y., Zhang, J., Gotardo, P.F.U., Lalonde, J.F.: What is a good day for outdoor photometric stereo? In: International Conference on Computational Photography (2015)
24. Horn, B.: Obtaining shape from shading information. Shape from Shading pp. 123–171 (1989)
25. Horn, B.K.P. (ed.): Robot Vision. MIT Press, Cambridge, MA, USA (1986)
26. Ikehata, S.: CNN-PS: CNN-based photometric stereo for general non-convex surfaces (2018)
27. Ju, Y., Tozza, S., Breuß, M., Bruhn, A., Kleefeld, A.: Generalised perspective shape from shading with oren-nayar reflectance. In: Proc. 24th British Machine Vision Conference. pp. 42.1–42.11. BMVA Press (2013)
28. Khanian, M., Boroujerdi, A.S., Breuß, M.: Photometric stereo for strong specular highlights. Computational Visual Media **4**, 83–102 (2018)
29. Kimmel, R., Siddiqi, K., Kimia, B.B., Bruckstein, A.M.: Shape from shading: Level set propagation and viscosity solutions. International Journal of Computer Vision **16**(2), 107–133 (1995)
30. Kozera, R.: Existence and uniqueness in photometric stereo. Applied Mathematics and Computation **44**(1), 1–103 (1991)
31. Lambert, Johann Heinrich Klett, M.J., Detlefsen, C.P.: Photometria Sive De Mensura Et Gradibus Luminis, Colorum Et Umbrae. Klett, Augustae Vindelicorum , ; Augustae Vindelicorum (1760)
32. Mecca, R., Falcone, M.: Uniqueness and approximation of a photometric shape-from-shading model. SIAM Journal on Imaging Sciences **6**(1), 616–659 (2013)
33. Mecca, R., Tankus, A., Wetzler, A., Bruckstein, A.M.: A direct differential approach to photometric stereo with perspective viewing. SIAM Journal on Imaging Sciences **7**(2), 579–612 (2014)
34. Oren, M., Nayar, S.K.: Generalization of the Lambertian model and implications for machine vision. International Journal of Computer Vision **14**(3), 227–251 (1995)
35. Phong, B.T.: Illumination for computer generated pictures. Communications of the ACM **18**, 311 – 317 (1975)
36. Quéau, Y., Mecca, R., Durou, J.D., Descombes, X.: Photometric stereo with only two images: A theoretical study and numerical resolution. Image and Vision Computing **57**, 175–191 (2017)
37. Quéau, Y., Durou, J.D., Aujol, J.F.: Normal integration: A survey. Journal of Mathematical Imaging and Vision **60**(4), 576–593 (2017)

38. Radow, G., Hoeltgen, L., Quéau, Y., Breuß, M.: Optimisation of classic photometric stereo by non-convex variational minimisation. Journal of Mathematical Imaging and Vision **61**(1), 84–105 (2019)
39. Ragheb, H., Hancock, E.R.: Surface radiance correction for shape from shading. Pattern Recognition **38**(10), 1574–1595 (2005)
40. Santo, H., Samejima, M., Sugano, Y., Shi, B., Matsushita, Y.: Deep photometric stereo network. In: Proceedings of the IEEE International Conference on Computer Vision. pp. 501–509 (2017)
41. Shi, B., Mo, Z., Wu, Z., Duan, D., Yeung, S.K., Tan, P.: A benchmark dataset and evaluation for non-Lambertian and uncalibrated photometric stereo. IEEE Transactions on Pattern Analysis and Machine Intelligence **41**(2), 271–284 (2019)
42. Stocchino, G.: Mathematical Models and Numerical Algorithms for Photometric Stereo (Modelli Matematici e Algoritmi Numerici per la Photometric Stereo). Bachelor's Thesis in Mathematics, University of Cagliari (2015), available at http://bugs.unica.it/gppe/did/tesi/15stocchino.pdf
43. Taniai, T., Maehara, T.: Neural inverse rendering for general reflectance photometric stereo (2018)
44. Tankus, A., Kiryati, N.: Photometric stereo under perspective projection. In: Proceedings of the IEEE International Conference on Computer Vision. pp. 611–616 (2005). https://doi.org/10.1109/ICCV.2005.190
45. Torrance, K.E., Sparrow, E.M.: Theory for off-specular reflection from roughened surfaces. J. Opt. Soc. Am. **57**(9), 1105–1114 (1967), http://www.osapublishing.org/abstract.cfm?URI=josa-57-9-1105
46. Tozza, S., Mecca, R., Duocastella, M., Bue, A.D.: Direct differential photometric stereo shape recovery of diffuse and specular surfaces. Journal of Mathematical Imaging and Vision **56**(1), 57–76 (2016)
47. Tozza, S., Falcone, M.: A comparison of non-lambertian models for the shape-from-shading problem. In: Perspectives in Shape Analysis. pp. 15–42. Mathematics and Visualization, Springer (2016)
48. Vanzi, M., Mannu, C., Dessì, R., Tanda, G.: Photometric stereo for 3D mapping of carvings and relieves. case studies on prehistorical art in Sardinia. In: Proceedings of Atti del XVII MAÇAO's Intemational Rock ArtSeminar (2016)
49. Woodham, R.J.: Photometric stereo: A reflectance map technique for determining surface orientation from image intensity. In: Optics & Photonics (1979)
50. Woodham, R.J.: Photometric method for determining surface orientation from multiple images. Optical Engineering **19**(1) (1980)
51. Yi, J., Ni, H., Wen, Z., Liu, B., Tao, J.: CTC regularized model adaptation for improving LSTM RNN based multi-accent Mandarin speech recognition. In: 2016 10th International Symposium on Chinese Spoken Language Processing (ISCSLP). pp. 1–5 (2016)
52. Zhang, R., Tsai, P.S., Cryer, J., Shah, M.: Shape from shading: A survey. IEEE Transactions on Pattern Analysis and Machine Intelligence **21**, 690–706 (1999)